Seismic faults triggered early stage serpentinization of peridotites from the Samail Ophiolite, Oman

Author(s):
Aupart, Claire; Morales, Luiz; Godard, Marguerite; Jamtveit, Bjørn; Oman DP Science Team

Publication date:
2021-11-15

Permanent link:
https://doi.org/10.3929/ethz-b-000505041

Originally published in:
Earth and Planetary Science Letters 574, https://doi.org/10.1016/j.epsl.2021.117137

Earth and Planetary Science Letters 574 (2021) 117137

Contents lists available at ScienceDirect

Earth and Planetary Science Letters

www.elsevier.com/locate/epsl

Seismic faults triggered early stage serpentinization of peridotites from the Samail Ophiolite, Oman

Claire Aupart [a,*], Luiz Morales [b,c], Marguerite Godard [d], Bjørn Jamtveit [a], the Oman DP Science Team

[a] Physics of Geological Processes (PGP), The Njord Centre, Dept. of Geosciences, University of Oslo, PO Box 1048, N-0316, Oslo, Norway
[b] Scientific Center for Optical and Electron Microscopy (ScopeM), ETH Zürich, Otto-Stern-Weg 3, 8093, Zürich, Switzerland
[c] Geological Institute, Department of Earth Sciences, ETH Zürich, Sonneggstrasse 5, 8092, Zürich, Switzerland
[d] Géosciences Montpellier, CNRS, University of Montpellier, Montpellier, France

ARTICLE INFO

Article history:
Received 16 October 2020
Received in revised form 5 July 2021
Accepted 27 July 2021
Available online 3 September 2021
Editor: A. Webb

Keywords:
fracturing
serpentinization
Oman ophiolite
Oman Drilling Project

ABSTRACT

Serpentinization of mantle peridotites has first order effects on the rheology and tectonic behavior of the oceanic lithosphere, on the global water cycle, and on the biosphere at mid-oceanic ridges. Investigating serpentinization of abyssal peridotites is limited by the scarce occurrences of peridotites at or close to the ocean floor at slow and ultra-slow ridge environments where peridotite is exposed by long-lived detachments. The processes controlling hydration of the upper mantle below a thick magmatic crust at fast spreading ridges are poorly constrained. Here we present results based on samples from cores drilled in peridotites from the Samail ophiolite obtained during the Oman Drilling Project. We describe an early generation of highly localized brittle faults ubiquitous through all the peridotite cores and investigate their relation to the main serpentinization event represented by mesh-textured serpentinites. We combine microstructural observations with mineral and bulk chemical analyses as well as oxygen isotope microanalyses obtained by secondary ion mass spectrometry (SIMS). Asymmetric wall rock damage, weakening of crystal preferred orientation (CPO) in small fault clasts, and intense fragmentation within the fault zones even in association with very small displacements suggest that the early stage faults represent seismic events and predate mesh formation. Hydration and mesh texture formation follows in the wake of this faulting. Serpentinization is associated with moderate enrichment of fluid mobile elements including B, Li, Rb and U, indicative of fluid rock interaction characterized by relatively low fluid/rock ratios. This is consistent with a scenario where serpentinization took place below a thick magmatic crust following an earthquake-induced permeability increase. The oxygen isotope compositions of mesh serpentine are consistent with off-axis serpentinization at temperatures in the range 200-250 °C

1. Introduction

Hydrothermal circulation within the oceanic lithosphere has first order effects on its thermal evolution (e.g. Schuiling, 1964; Stein and Stein, 1994), and on the mass-transfer between the oceans and the solid Earth (e.g. Paulick et al., 2006). Serpentinization involves hydration of olivine and pyroxene and their replacement by serpentine and other hydrous minerals, and leads to major changes in the physical and chemical properties of the lithosphere (e.g. Escartin et al., 2001; Malvoisin, 2015). It also affects the biological activity at the seafloor (e.g. Holm and Charlou, 2001). Whereas fluid circulation in the shallow oceanic crust is extensively studied and characterized (e.g. Fisher, 1998; Tolstoy et al., 2008), the extent and nature of fluid migration in the lower crust and upper mantle is less well constrained.

Serpentinization of mantle peridotites is mainly studied at slow to ultra-slow ridge settings where mantle rocks are brought to the seafloor by large scale detachment faults along "magma-starved" portions of ridge (Cannat, 1993). In such settings, the extent of serpentinization is very extensive (Bach et al., 2004) and features formed during the incipient stages of peridotite hydration at depth are largely overprinted. However, petrographic studies highlight the important role of thermal cracking and tectonic stresses (e.g. Boudier et al., 2005). Moreover, seismic data from ultra-slow ridges suggest that earthquake-related brittle fracturing may play a key role in the generation of the permeability required to bring ocean water in contact with mantle peridotites (Aupart, 2020). The processes involved in serpentinization of peridotites at mantle depths

* Corresponding author.
E-mail address: c.o.m.aupart@geo.uio.no (C. Aupart).

https://doi.org/10.1016/j.epsl.2021.117137

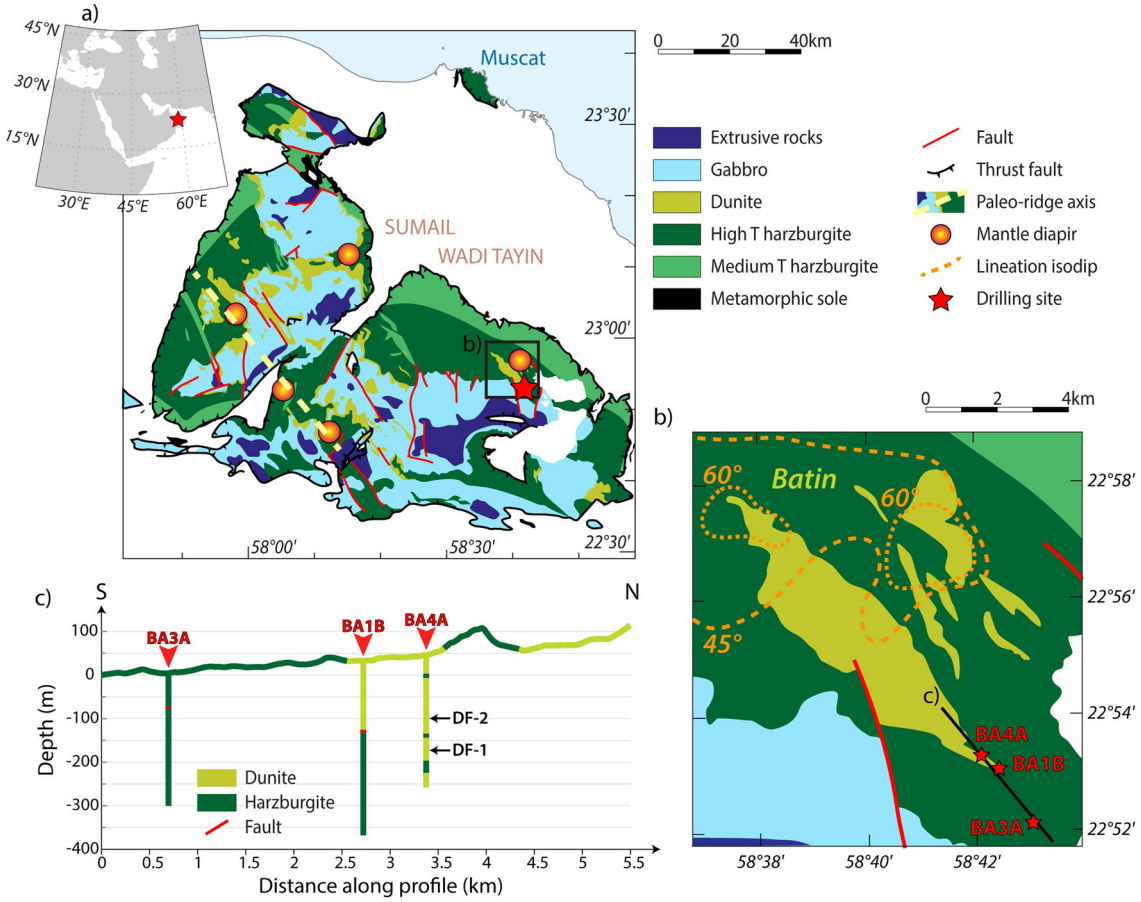

Fig. 1. a) Map of the Southern part of the Samail ophiolite showing the location of the Oman DP BA site (after Nicolas et al., 2000) and the approximate inferred position of the fossil ridge axis and mantle diapirs based on structural observations (after Boudier et al., 1997). b) Map of the Batin dunite area showing the location of the three drill holes where cores were recovered during the Oman Drilling Project (after Noël, 2018). The legend is the same as in a). Lineation isodips (after Ildefonse et al., 1993) indicate the approximate location of the diapir at the North-West of the Oman DP drilling sites. c) Profile showing the relative location of the three recovered cores and location of the two main samples presented in this study. (For interpretation of the colors in the figure(s), the reader is referred to the web version of this article.)

associated with fast-spreading ridges are harder to constrain as mantle rocks are covered by ca. 6 km of basaltic crust and direct sampling by Ocean Drilling at these depths has not yet been performed. An alternative approach is to study fragments of oceanic crust emplaced onto continental crust during plate convergence, i.e. ophiolites.

Here we describe highly localized brittle faults through dunite and harzburgite in the Samail ophiolite based on a study of drill cores obtained through the Oman Drilling Project. We focus on the earliest stages of faulting, which we interpret to have occurred during the incipient stages of serpentinization and hydrothermal activity.

2. Geological setting

2.1. The Batin dunite area

The Samail ophiolite is located on the eastern corner of the Arabic peninsula (Fig. 1a) and covers an area ca. 500 km long and 60 km wide along the coast. The lithospheric section is up to approximately 20 km thick with the typical structure and composition associated with fast spreading ridges. Remarkably, the paleo-ridge axis seems to have been preserved (Boudier et al., 1997; Fig. 1a). Former oceanic lithosphere overlays an amphibolite grade metamorphic sole with an inverted temperature gradient. The ages of the metamorphic sole and the crust indicate that the rocks composing the ophiolite were formed and obducted between 96-95 Ma (Rioux et al., 2016) during the closure of the Neo-Tethys ocean.

The Batin dunite is a 10 km long and 2.5 km wide tabular dunitic lens located in the southernmost massif of the Oman ophiolite (Fig. 1a) in the upper part of the mantle section, close to the mantle-crust transition. Dunite is believed to form by dissolution of orthopyroxene from harzburgite during interaction with basaltic melt (Kelemen et al., 1997). The Batin dunite is thus considered to be a zone of melt accumulation. This observation, in addition to plunging mantle lineations (Fig. 1b), led Nicolas et al. (1988) to interpret the area as a former mantle diapir feeding the former ridge axis with magma. However, while normal diapirs are normally located below the ridge axis, like the ones observed along the East Pacific Rise (Toomey et al., 2007) and most of the other mantle diapirs identified in Oman (Fig. 1a), the Batin diapir is an off-axis diapir located ca. 50 km from the ridge axis.

The Batin region is tectonically complex. Many generations of faults crosscut the area. Some of them are associated with the emplacement of the off-axis diapir into the cold lithosphere as is observed in the Mansah diapir, also in Oman (Jousselin and Nicolas, 2000). Other faults likely formed during the emplacement of the ophiolite on the continental lithosphere, but the largest ones seem to have formed during the formation of the oceanic lithosphere. Indeed, similar faults in the neighboring Samail massif were interpreted as syn-magmatic by Rospabé et al. (2019) and hence have formed while the ridge axis was still active. Another study by Zihlmann et al. (2018), conducted in the same massif as the BA site on a fault parallel to the set of major faults observed in the Batin region, recognized these lithospheric faults as major

fluid pathways controlling the hydrothermal alteration of the lower crust and eventually uppermost mantle.

2.2. The Oman Drilling Project - active alteration cores

Samples in this study come from drill cores produced during the second drilling phase of the Oman Drilling Project (Oman DP; https://www.omandrilling.ac.uk/) during the winter 2017-2018. The Active Alteration (BA) site is located at the southeast end of the Batin dunite lens area (Fig. 1b). Seven holes were drilled including three recovered cores at Holes BA1B, BA3A and BA4A. Thorough descriptions of these cores (a total of 1000 m) made onboard of the research vessel Chikyu during summer 2018 are available in an IODP report (Kelemen et al., 2020). Summary logs of the cores are provided in Supplementary Fig. S1.

The cores are ca. 300 m (BA3A and BA4A) and 400 m long (BA1B) and located within or near the Batin dunite body (Fig. 1c). BA4A is mostly composed of dunite and located at the tip of the Batin dunite. The upper 160 m of BA1B are composed of dunite, likely belonging to the same body as BA4A. A 3-meters wide fault zone separates the dunitic part from the underlying 240 m, mostly composed of harzburgite. This major fault may be of the same type as the syn-magmatic hydrothermal faults described by Rospabé et al. (2019) and Zihlmann et al. (2018). However, a thorough study would be required to verify this assertion. BA3A is located outside the Batin dunite lens and is mostly composed of harzburgite. The three cores display very high degrees of serpentinization (above 80%) both as pervasive alteration and in veins. All cores are crosscut by a number of dykes, most of them with a gabbroic or clinopyroxenitic composition. These dykes have highly variable degrees of alteration but are never completely fresh. Clinopyroxene is locally preserved. Deformation within the BA cores is relatively abundant and mainly brittle. Apart from a decrease in the number of open cracks and cataclastic zones within the weathering profile, deformation structures do not have a specific repartition pattern. The fault zone separating the dunitic and harzburgitic parts in BA1B is the only large scale deformation feature that has been reported in the cores.

In the following, we focus on one specific type of fault that has been observed during the description of the BA cores by the Oman DP scientific team. Even though the samples we describe are strongly serpentinized, we refer to their original lithologies as their rock type. However, any mineral description refers to the current mineralogy of the samples.

3. An early family of faults

3.1. Fault zone characteristics

The oldest generation of faults identified in the Samail peridotites are dark sealed faults and associated cataclastic bands. They are present in all the cores and do not appear to be restricted to a specific depth. However, due to their discreet appearance in the cores, the exact repartition of these faults is unknown. They seem to be an early feature as they crosscut dykes but are crosscut by most of the other structures (e.g. open cracks, veins). They represent single events with no trace of reactivation. Faults are generally relatively thin (several millimeters at most) compared to the displacement they induced (up to several centimeters). However, not all the faults are associated with centimeter-scale displacement, it can be much smaller (sometimes less than one millimeter). We refer to these faults as “dark faults” in the following.

In this study, we compare two samples representing two different stages of the dark faults development. Sample DF_1 is crosscut by a series of thin dark fractures or faults with very small displacements (less than a millimeter; Fig. 2a-b). It comes from one of the freshest dunitic parts of the BA cores. The sample is still associated with a high degree of serpentinization (>90%), but olivine relics are locally common and particularly concentrated in the central parts of unfractured domains (Fig. 2b). The internal part of the fractures is characterized by intense fragmentation (Fig. 2c). Sample DF-2 is crosscut by a dark fault associated with ca. 6 cm displacement (Fig. 2d). The dunitic sample is completely serpentinized. The internal part of the fault zone is developed into a cataclasite with clasts embedded in a fine-grained serpentine matrix (Fig. 2e). The deformation is mostly contained within the cataclastic zone, but some strain is accommodated by microfracturing and small-scale faults in the wall-rock. The wall-rock damage is asymmetrically distributed with one side (thin sections’ top sides in Fig. 2e) more damaged than the other. While the wall-rock contact with the main cataclastic zone is sharp on the least damaged side, it is more complex and gradual on the most damaged side. In both samples, the main dark fault is sub-vertical and can be followed over more than one meter within the cores.

The dark fault in sample DF-2 crosscuts a gabbroic dyke. This dyke contains clinopyroxene that has been partially preserved from alteration and provides an opportunity to characterize fault deformation. Two electron backscatter diffraction (EBSD) maps were obtained from a zone of the DF-2 cataclasite where remnant clinopyroxene clasts from the dyke are abundant. Details on the sample preparation and acquisition method are provided in Appendix A. The first orientation map (DF-2_map_1) was carried out in a domain containing rather large clasts of clinopyroxene, whereas the second map (DF-2_map_2) was carried out in a smaller area containing a large number of fine-grained clasts (orientation maps location is given in Fig. 3). Data was processed using the MatLab toolbox MTEX (version 5.2.8; http://mtex-toolbox.github.io; Bachmann et al., 2010, 2011; Hielscher and Schaeben, 2008). A misorientation threshold of 10° was applied during grain modeling and detected grains with less than 10 pixels were not considered in our calculations. Clinopyroxene orientation maps are provided in Supplementary Fig. S2.

The largest clasts in the large-grained domain show a relatively strong crystal preferred orientation (CPO; upper pole figures in Fig. 3c) with two maxima, which are likely to be inherited from the original grains’ orientations before faulting. However, when we consider all the grains in the map, the orientation of (100), (010) and [001] have a *quasi*-uniform distribution (Fig. 3c) even though traces of the pre-faulting CPO are still visible in the intermediate-sized clasts (two central rows of pole figures in Fig. 3c). The grain size area (2-D) distribution from domain DF-2_map_1 follows a well-defined power law with a slope of 1.77 (Fig. 4a). In contrast, the grain size distribution from DF-2_map_2 is best fitted by a lognormal distribution (Fig. 4b). The difference in distribution between the two EBSD maps is likely due to a higher alteration degree of the small grains from DF-2_map_2. Indeed, because their larger surface area to volume ratio, small grains are more altered than large ones. Finally, the Shape Preferred Orientation (SPO) of the grains was extracted from the EBSD maps (Fig. 4c). Both maps show a SPO oriented around 110-120° from the orientation of the dark fault. Interestingly, a secondary SPO parallel to the dark fault orientation can be observed in the results from DF-2_map_2.

3.2. Geochemistry of mesh textured serpentinite

The peridotites from the BA cores show extensive and pervasive serpentinization. Whole rock trace element compositions are within the range of results previously obtained for Oman peridotites (Supplementary Fig. S3 & Tables S2-S3; methods in Appendix B) with moderate enrichment of the fluid mobile elements U, Rb and Sr when normalized to primitive mantle (Godard et al., 2000; Hanghøj et al., 2010; Sun and McDonough, 1989). Olivine

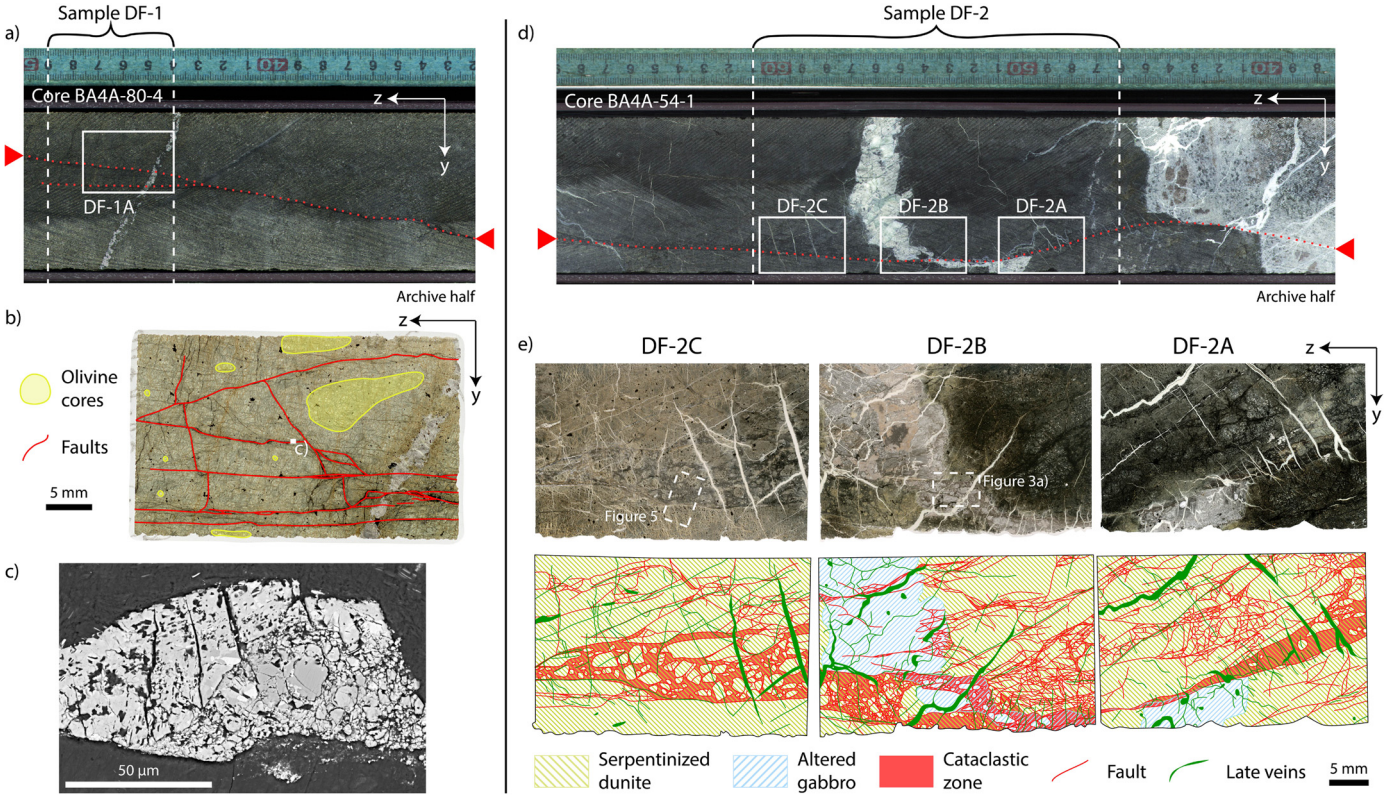

Fig. 2. Samples DF-1 and DF-2. a) Core image of sample DF-1. The white rectangle indicates the location of the thin section DF-1A. b) Transmitted light picture of the thin section DF-1A. The positions of the dark faults and of zones where olivine relicts can be found are indicated in red and yellow, respectively. c) Scanning Electron Microscopy (SEM) picture of an altered and fragmented chromite grain inside one of sealed cracks constitutive of the dark fault in DF-1. The position of the picture is indicated in b). d) Core image of sample DF-2. The white rectangles indicate the location of thin sections DF-2A, DF-2B, and DF-2C. b) Transmitted light pictures and schematic drawings of the three thin sections DF-2A, DF-2B, and DF-2C. The late veins represented in green are not treated in this study. In all figures, the z direction points towards the bottom of the core. In a) and d) a red dashed line shows the position of the dark faults.

has been replaced during serpentinization by a well-developed mesh texture composed of mesh veins that form a network of serpentine veins, and mesh cores. We have not analyzed the serpentine polymorph composing the mesh veins in DF-1 and DF-2, but X-ray analyses made during Oman DP on similar samples (Kelemen et al., 2020) and optical properties strongly suggest it is lizardite. Mesh cores are composed of olivine remnants or alteration phases dominated by serpentine. The composition and structure of the mesh cores are highly variable. Magnetite is rare within the mesh texture but occurs as numerous micrometric grains within the cataclastic matrix.

In samples DF-1 and DF-2 the mesh veins form a network of two almost perpendicular sets. In both cases the most developed set of veins is sub-perpendicular to the dark faults. In sample DF-2, where the dark fault is well developed as a cataclastic zone, the mesh texture is present both in the wall-rocks and in the largest clasts in the cataclasite. The orientation of the veins as well as the crystallographic orientation of serpentine inside the veins appear continuous from the wall-rock through the cataclastic zone clasts (Fig. 5). This reflects limited clast rotation after mesh formation.

Oxygen isotope compositions and boron concentration were measured *in-situ* (in thin section DF-2C) by SIMS within the mesh veins (in the wall-rock and in the clasts), as well as in the cataclastic matrix in the fault zone (Table 1; see methods in Appendix C). Oxygen isotopes compositions are in the range of oceanic serpentine (e.g. Mével, 2003). δ^{18}O-values in the mesh veins from the wall-rock and from the clasts can both be divided into two groups. Group 1 is mostly represented by thick veins oriented sub-perpendicular to the fault zone (cyan color in Fig. 5). This population has δ^{18}O-values between 2.72‰ and 4.95‰ with a mean of 3.75‰. Group 2 is composed of thin veins, often oriented sub-parallel to the strike of the dark fault (orange color in Fig. 5) and has higher δ^{18}O-values between 5.92‰ and 6.55‰ with a mean of 6.27‰. δ^{18}O-values in the dark fault clasts show similar behavior. The thick fault-normal mesh veins in the clasts (Group 1) all belong to the low δ^{18}O-value population (between 1.18‰ and 3.10‰ with a mean of 2.18‰), while high δ^{18}O-values (between 7.19‰ and 7.68‰ with a mean of 7.44‰) are only reported in thin veins (Group 2). The dark fault matrix shows limited variations in its δ^{18}O values between 4.99‰ and 5.76‰ with a mean value of 5.35‰. The boron concentrations in the wall-rock mesh veins vary from 2.0 ppm to 10.4 ppm with a mean value of 5.2 ppm, while the boron concentrations in the clasts mesh veins vary from 1.2 ppm to 8.2 ppm with a mean value of 4.8 ppm. There is in consequence no major difference between the boron content in the mesh veins from the wall-rock and from the fault zone clasts. There is no significant correlation between oxygen isotopes and boron concentrations.

A striking feature of the mesh cores observed in this study is a pronounced oscillatory zoning pattern. In sample DF-1, serpentinized mesh cores are most common close to the early stage dark fractures (Fig. 2b). These mesh cores appear colorless under optical light, but chemical maps reveal that they are characterized by alternating silica and iron rich layers (Fig. 6a). Magnesium is evenly distributed inside the mesh cores and sulfide grains are rare. In sample DF-2, mesh cores located around and within the main dark fault share some similarities with the patterns observed in sample DF-1, indicative of a similar formation process, but also some significant differences. In plane-polarized light, their color varies from brown, associated with well-defined zoning patterns, to black, showing no obvious structure. This evolution from brown to black is mostly visible in the wall-rock close to the dark fault,

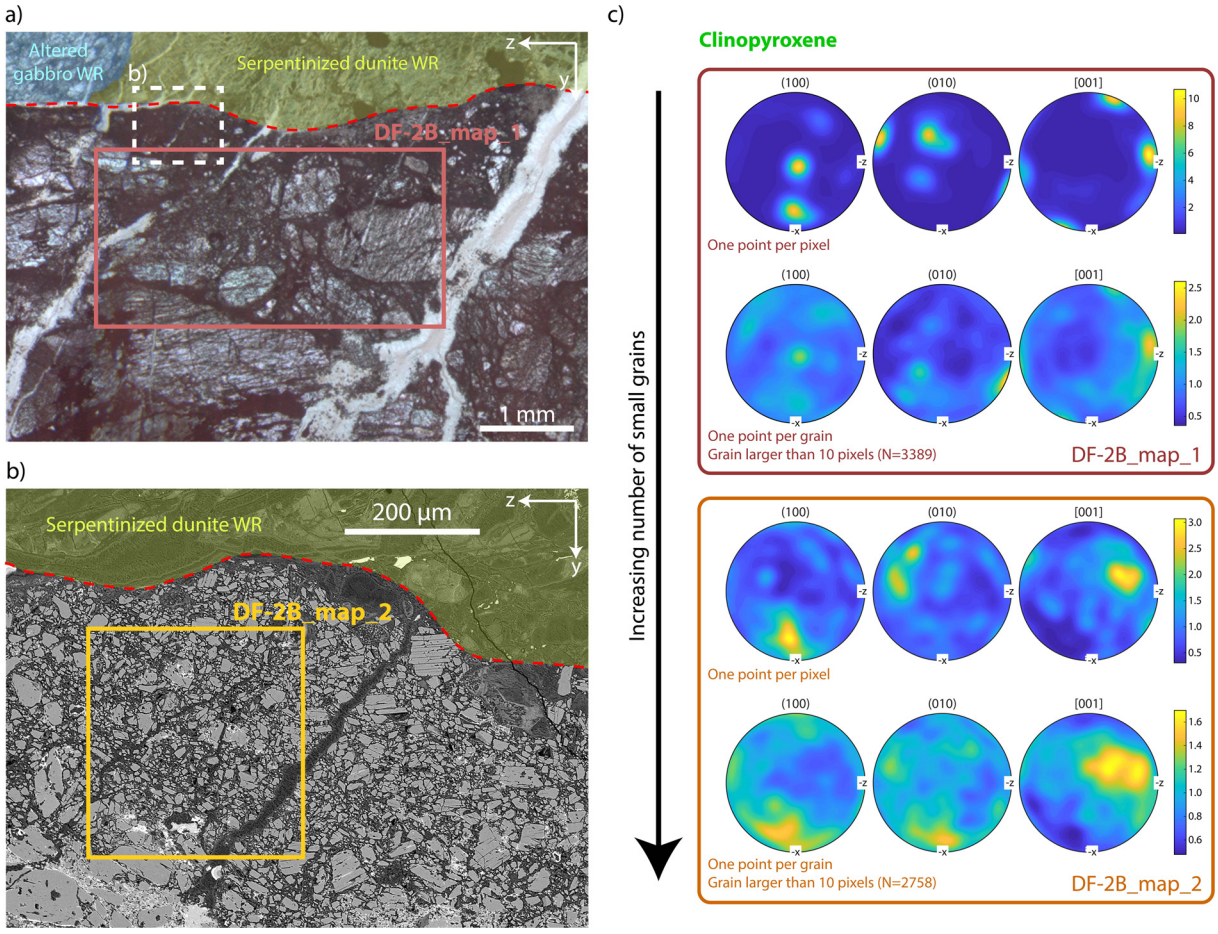

Fig. 3. a) Optical microphotograph and b) backscattered electron (BSE) image indicating the location of the EBSD maps within the cataclastic zone of the dark fault in thin section DF-2B. Location of picture a) is given in Fig. 2e. c) Pole figures showing the distribution of the poles to the (100) and (010) planes, and of the [001] axes of clinopyroxene. For each map, the upper pole figures give the crystallographic orientation obtained considering all the pixels of the EBSD map, thus dominated by the largest grains. The lower pole figures are obtained considering a mean crystallographic orientation for each crystal grain, consequently better reflect the effect of smaller grains (more numerous) on the CPO of these two samples. N is the number of grains used to determine the CPO. The x, y, and z directions are the same as defined in Fig. 2, density calculations performed assuming a halfwidth of 10°. Orientation maps are provided in the Supplements (Fig. S2).

but also in some of the large clasts, where the clast cores show lighter and better-defined patterns than their rim. The brown patterns have a structure similar to the patterns observed in the sample DF-1, but their chemical composition is different (Fig. 6b). The silica-iron layering is still very prominent, but magnesium and sulfur (as sulfide grains) are enriched in the iron-rich, silica-poor, layers. These changes are increasingly striking as the mesh cores become darker and the layering less defined as in Fig. 6c.

Major elements measurements by electron microprobe were made in the mesh veins, in the mesh cores, both in the wall-rock and in the fault zone clasts, and in the cataclasite matrix (Supplementary Tables S4-S8; methods in Appendix D). These analyses were made in thin section DF-2C. Mesh veins (both in the wall-rock and in the clasts) and the cataclasite matrix have rather homogeneous serpentine compositions. Mesh cores in the wall-rock as well as in the clasts show much more variation (Fig. 7a). Two trends can be distinguished within the mesh cores composition. The first trend (blue arrows in Figs. 7) is characterized by a decrease in silica and is mainly represented by the mesh cores in the wall-rock. It is associated with a decrease in the totals, reaching values as low as 75% for samples with less than 5wt% SiO_2 (Fig. 7b). This is consistent with a composition dominated by brucite. The second trend (orange arrows in Figs. 7) is associated with an increase of iron content and is mainly represented by mesh cores in the clasts. It is associated with sulfur enrichment and totals up to 100% (Fig. 7b). This trend is consistent with a high Fe-sulfide content. We observe a positive correlation between sulfur and alumina contents in all the measurements. The wall-rock and clasts cores have the highest Al and S concentrations, but a slight increase in Al and S concentrations in the clasts mesh veins and the cataclasite matrix is also observed compared to the wall-rock mesh veins (Supplementary Fig. S5).

4. A conceptual model of serpentinization

4.1. Early stage faulting

Our observations indicate an intimate link between deformation and serpentinization. The orientation of the mesh veins in sample DF-2 is the same in the wall-rock and in the dark fault's clasts independent of their size (Fig. 5). This is consistent with the main hydration event occurring after the faulting. Moreover, we remark that in both samples DF-1 and DF-2 the orientation of the most developed set of mesh veins is approximately perpendicular to the dark faults. This highlights a possible link between faulting and mesh vein formation. Finally, in sample DF-1, the olivine relics in mesh cores are located exclusively at some distance from the early stage dark fractures (Fig. 2b), indicating that mesh core replacement is also linked to the occurrence of these early stage brittle features.

The dark faults are associated with intense fragmentation, even when displacement is limited as it is the case with sample DF-1

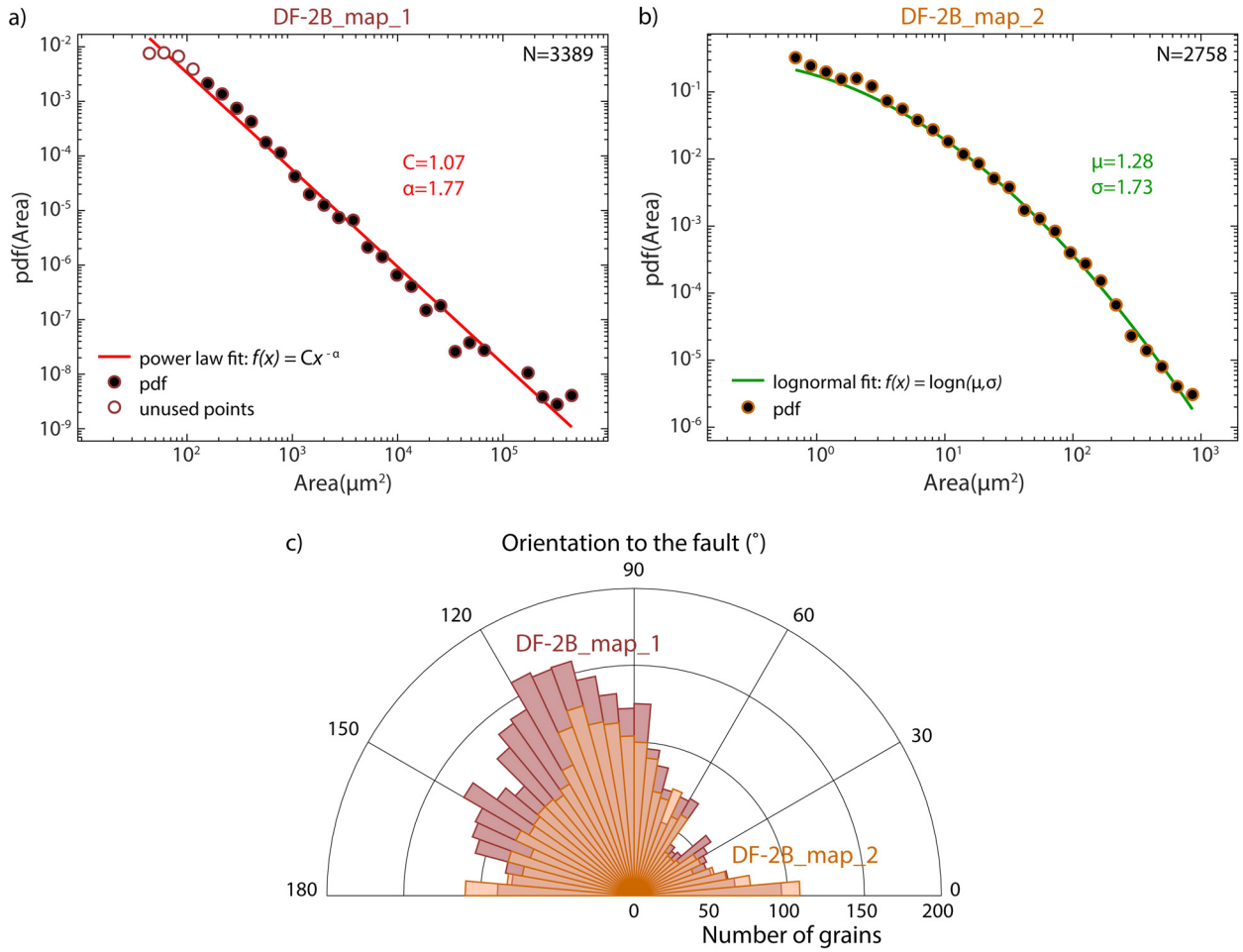

Fig. 4. Grain size distributions and shape orientations of clinopyroxene clasts obtained from the EBSD maps. Grain size distributions are defined by the probability density functions (pdf) of the grain cross-section areas. The pdf returns the probability to encounter a grain of given area. Grain size distributions are fitted following the same method as used in Aupart et al. (2018). Only grains larger than 10 pixels are used. a) Grain size distribution from the large-scale map (DF-2_map_1) presented in Fig. 3a. The distribution is well fitted by a power law, described by two parameters α and C. α is the slope of the power law, describing the proportion of large grains to small grains, and C a scaling coefficient, depending on the grain spatial density. b) Grain size distribution from the small-scale map (DF-2_map_2) presented in Fig. 3b. The distribution is best fitted by a lognormal distribution that is described by two parameters μ and σ. μ is linked to the median of the distribution while σ is related to the spread of the distribution. c) Rose diagram showing the distribution of the shape orientation of the grains in DF-2_map_1 and DF-2_map_2. In this diagram the dark fault is oriented sub-parallel to a 0° orientation. In a) and b) N is the total number of grains used in the grain size and shape orientation distributions.

(Fig. 2c). This observation suggests an energetic, possibly seismic, event. The sharp fault edges and asymmetric wall-rock damage (Fig. 2e) support this hypothesis. The power law scaling exponent of ca. 1.8 in the grain size area distribution (= 2.6 for the radii distribution; Fig. 4a) of the dark fault clasts from sample DF-2 is similar to the value obtained by Sammis et al. (1987) and Steacy and Sammis (1991) for fragmentation during grinding in seismic fault zones. The size dependent rotation of the clasts indicated by the weakening of the CPO with decreasing grain size (Fig. 3c) and the development of a SPO (Fig. 4c; Cladouhos, 1999) also point towards intense brittle deformation.

Our observations stress that early faulting plays a major role in the initiation of serpentinization by initiating the supply of fluids to initially dry mantle peridotites. The systematic orientation of the main mesh veins subperpendicular to the dark faults may indicate that the tectonic stress responsible for the faulting also affects the mesh orientation.

4.2. Conditions of serpentinization

We observe moderate enrichments in U, Rb, Li and B in our samples (Supplementary Fig. S3a) typical of serpentinization in an oceanic environment (Deschamps et al., 2011). The FME concentrations we observe are lower than typical abyssal peridotite signature (that have undergone extensive interaction with seawater at the seafloor; Peters et al., 2017) but consistent with depleted peridotites drilled along the Mid-Atlantic Ridge (that have been less exposed to seafloor alteration) (Supplementary Fig. S6; Godard et al., 2008; Paulick et al., 2006). These results are thus consistent with fluid-rock interactions occurring at a certain depth below the seafloor and relatively low water-rock ratio (Agranier et al., 2007).

The mesh veins and the matrix cataclasite have relatively homogeneous compositions, coherent with pure serpentine (Fig. 7a). The oxygen isotope analyses, made in these phases, can be interpreted in terms of temperature of serpentinization (Saccocia et al., 2009). The oxygen isotope composition of serpentine formed by hydration of a peridotite protolith depends on the temperature and fluid composition. The fluid composition may range from seawater ($\delta^{18}O = 0‰$) to positive values for hydrothermally altered water. If a thick oceanic crust was covering the peridotite at the time of serpentinization it is likely that the fluid composition was modified by fluid-rock interactions when reaching the cooling peridotites. Temperatures of serpentinization obtained by assuming that seawater was the serpentinizing fluid are in the range 200-250 °C (Table 1). For hydrothermally altered waters with a $\delta^{18}O$-value of 2.4‰ (representative composition obtained by Campbell et al.

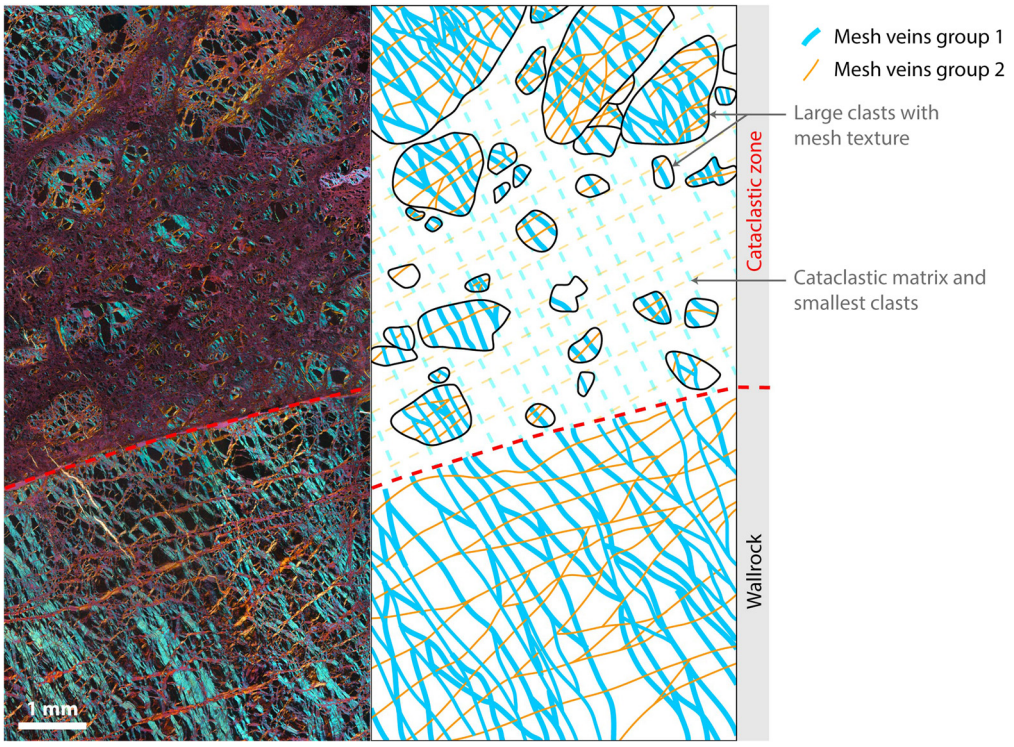

Fig. 5. Microphotograph from the thin section DF-2C using the optical microscope's gypsum plate (location indicated in Fig. 2e) and associated schematic representation. Mesh veins have either a cyan or orange color, which indicate two predominant crystal orientations approximately perpendicular to each other, common to the texture of serpentine derived from olivine. These two orientations correspond to the two mesh vein groups identified by oxygen isotopes analyses (Table 1 and Supplementary Fig. S4). The magenta color indicates isotropic or very fine-grained zones (here, mostly the cataclastic matrix). The dashed red line indicates the limit between the dark fault cataclastic zone (above) and the wall-rock (below).

Table 1
Oxygen isotope compositions and boron concentrations (ion probe analyses) made in thin section DF-2C. The location number refers to the different points analyzed. A detailed map of these is given in Supplementary Fig. S4. Temperatures are calculated based on Saccocia et al. (2009) and considering either seawater or a hydrothermally evolved fluid as the reactive fluid. In the calculation, a δ^{18}O-value of 0‰ is used for seawater and of 2.4‰ for hydrothermally evolved water (Campbell et al., 1988). WR = wall-rock.

Location number	δ^{18}O	± ‰	Temperature (°C) *reaction with seawater*	Temperature (°C) *reaction with hydrothermal water*	^{11}B/^{28}Si	Boron (ppm)		
1	3.68	0.23	242	296	0.17	5.4	Group 1	**Mesh veins WR**
2	4.95	0.24	219	266	0.20	6.5		
3	2.72	0.23	262	324	0.06	2.0		
4	3.79	0.23	240	294	0.16	5.1		
5	3.53	0.22	245	301	0.10	3.1		
6	3.35	0.21	249	305	0.13	4.1		
7	3.24	0.21	251	308	0.22	6.9		
8	4.24	0.23	231	282	0.32	10.4		
9	4.26	0.23	231	282	0.10	3.2		
10	6.34	0.22	197	237	0.19	6.2	Group 2	
11	6.55	0.22	194	233	0.12	3.8		
12	5.92	0.24	203	245	0.17	5.5		
13	1.18	0.24	299	377	0.07	2.4	Group 1	**Mesh veins clasts**
14	3.10	0.22	254	312	0.04	1.2		
15	2.25	0.23	272	338	0.26	8.2		
16	7.68	0.25	178	213	0.24	7.6	Group 2	
17	7.19	0.23	185	222				
18	5.40	0.24	211	256	0.15	4.9		**Matrix**
19	5.23	0.22	214	259	0.14	4.4		
20	5.76	0.23	206	248	0.25	7.9		
21	4.99	0.25	218	265	0.28	8.9		

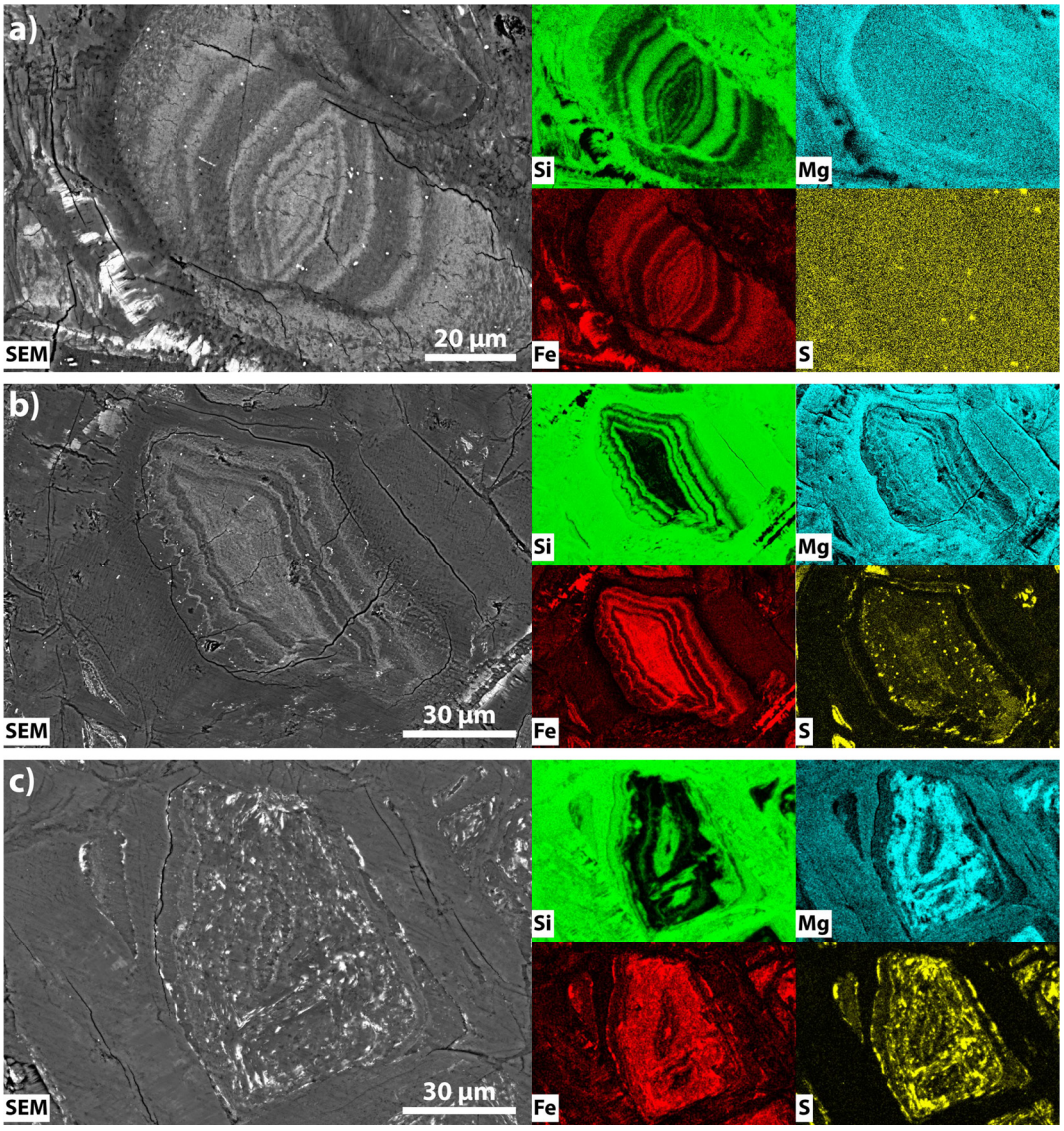

Fig. 6. Backscattered electron images and respective energy dispersive spectroscopy (EDS) maps (see methods in Appendix A) of mesh cores located in the wall-rock, close to a fracture in thin section DF-1A (a), a few millimeters from the main fault zone in thin section DF-2C (b), and close to the main fault zone in thin section DF-2C (c).

(1988) from the Snake Pit vent field), the estimated temperature of serpentinization is between ca. 250 and 300 °C (Table 1).

The range of observed δ^{18}O-composition for Group 1 and 2 mesh veins (Table 1) may reflect different temperatures of formation where the thin veins formed at 50-100 °C lower temperatures than the thicker ones. Mesh formation over such an extended temperature interval does, however, seem unlikely. More probably, this variation in δ^{18}O-values reflects variations in the local fluid compositions in fractures of different aperture and orientation, with more rock-dominated fluid compositions in thin fractures where fluid fluxes are lower. Assuming that Group 1 and Group 2 veins formed at similar temperatures, but from different pore fluid compositions (δ^{18}O-values of 0 and 2.4‰ respectively), implies that mesh vein formation occurred at 210-260 °C (Fig. 8). Since the B-content of the fluid is expected to be less sensitive to fluid-rock interactions, this is supported by the relatively constant B-concentration for all mesh veins (Table 1), irrespective of orientation. The obtained serpentinization temperature range is slightly higher than temperatures expected in the absence of magnetite in the mesh veins (Klein et al., 2014) but lower than the magnetite formation peak (around 300 °C; McCollom and Bach, 2009). It is also commonly observed that magnetite preferentially forms within the higher fluid flux pathways (e.g. Bach et al., 2006) this would be consistent with the preferential occurrence of magnetite in the matrix of the cataclastic zone that likely focused the highest fluid flux. The temperature formation of the mesh cores, usually considered to form later than the mesh veins as the system becomes more open (Viti and Mellini, 1998), is likely better constrained by the cataclastic matrix as, as representative of the main fluid pathway. Considering seawater as the reactive fluid suggests temperature estimates around 210 °C. This is broadly consistent with the brucite Mg# (cationic Mg/(Mg+Fe)) near 0.7-0.8 in the mesh cores as inferred from Fig. 7a (McCollom and Bach, 2009).

The BA site is located ca. 50 km from the fossil ridge axis. The temperatures estimated in this study are surprisingly low considering the position of the samples within the lithospheric section. Such temperatures could not be reached purely through conductive cooling of the lithosphere. However, numerous studies highlight the important role of hydrothermal cooling especially close to the ridge axis (e.g. Stein and Stein, 1994). Fast spreading ridges, such as the fossil Oman ridge, are usually not considered to be sites of extensive serpentinization due to their high temperatures. Nonetheless, it has been shown that formation of lithospheric scale hydrothermal cells can provide enough cooling for local serpen-

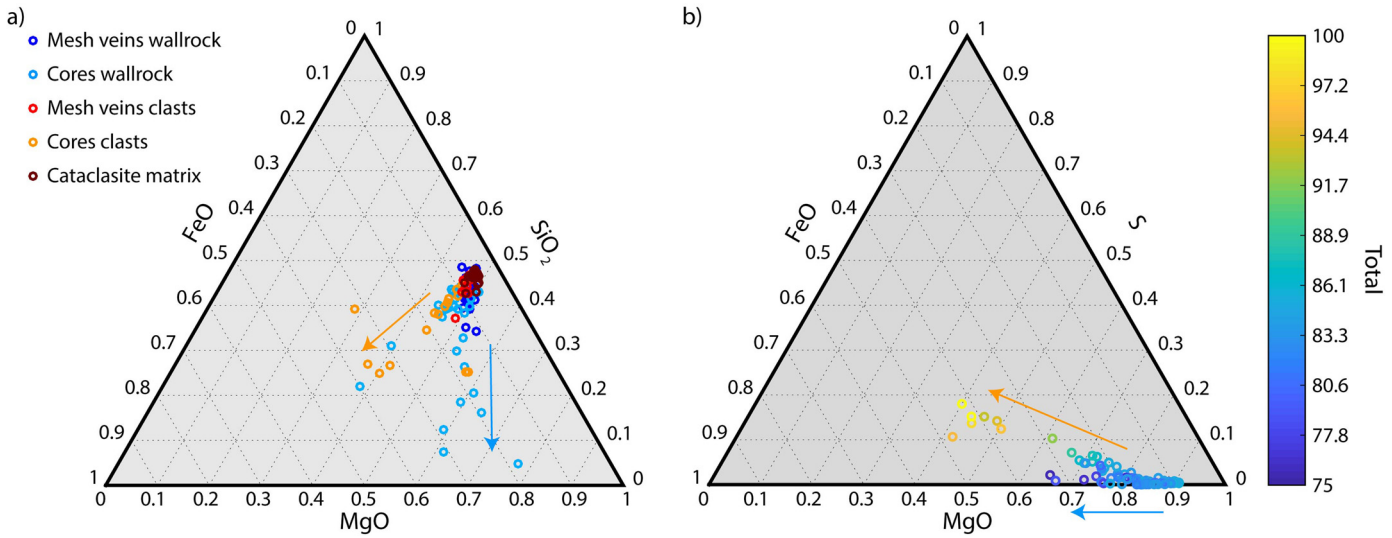

Fig. 7. Results from microprobe analyses of thin section DF-2C (Supplementary Tables S4-S8). a) MgO-SiO_2-FeO diagram showing the composition of different microstructural domains. b) MgO-S-FeO diagram showing the composition of the same data as in a) including the total percentage analyzed by the microprobe. In a) and b) the arrows show two trends recorded in the mesh cores. The figures are obtained based on wt%.

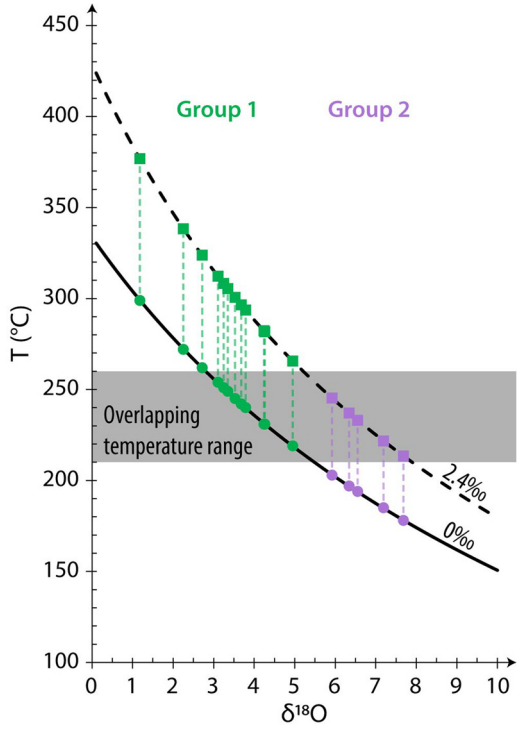

Fig. 8. Estimates of the serpentinization temperature for mesh veins based on oxygen isotopes. Curves represent the temperature estimates considering seawater (solid line; δ^{18}O-value of 0‰) or a hydrothermal fluid (dashed line; δ^{18}O-value of 2.4‰) as the reactive fluid. Temperatures have been calculated for both fluid types for Group 1 and Group 2 mesh veins.

tinization to occur at distances exceeding ca. 20 km from the ridge axis (Iyer et al., 2010). This is consistent with the BA drilling site being located approximately 50 km from the fossil ridge axis. It also means that the lithosphere sampled at the BA site could have been serpentinized at a shorter distance to the ridge axis than its current position relative to the ridge axis if conditions were favorable. The location and size of the large scale hydrothermal cells is likely controlled by the occurrence of major lithospheric faults such as those described by Zihlmann et al. (2018) and Rospabé et al. (2019) in Oman. The timing of the hydrothermal alteration associated with the lithospheric faults is constrained by the occurrence of hydrated melts reported by Rospabé et al. (2019). This demonstrates that the ridge was magmatically active at the onset of hydrothermal alteration. Additional support for this model is the occurrence of anhydrite, typical of alteration in an oceanic environment, reported by Mariani et al. (2019) within a core (also drilled during Oman DP) crosscutting the fault studied by Zihlmann et al. (2018). Some of these lithospheric faults are present in the Batin region and located close to the drilling site. As mentioned in Section 2.2, the meter-scale fault sampled by the core BA1B may also be one of these faults. Moreover, it is likely that the location of the sampling site at the periphery of an off-axis diapir enhanced hydrothermal activity in the region (Jousselin and Nicolas, 2000). The Batin region was thus a predisposed zone for extensive hydrothermal cooling to occur.

4.3. Stages of serpentinization

The formation of mesh veins and replacement of mesh cores is often considered to happen in two stages. Mesh veins form first, in a rock-dominated environment and under relatively closed system conditions (e.g. Viti and Mellini, 1998). Yet, pervasive formation of mesh textures requires “pervasive water supply”. Microcracking due to thermal contraction has been suggested as one possible contribution to pervasive permeability generation (Boudier et al., 2005). Considering that fracturing occurred first (step 1 in Fig. 9a), the circulation of cold seawater through the cracks could be the driving force for thermal cracking (step 2 in Fig. 9a). During this step, the volume increase associated with serpentinization is not compensated by transport of elements and reaction-induced fracturing (Plümper et al., 2012) is likely to occur (step 3 in Fig. 9a).

Replacement of olivine relics remaining in the mesh cores are believed to take place in a second step as the system progressively opens (Viti and Mellini, 1998). Preferred replacement of mesh cores in and around the early stage dark faults and fractures described here may reflect that they represent permeable pathways over a significant time interval also after the onset of initial mesh formation (step 4 in Fig. 9a). The formation of Liesegang-like oscillatory zoning pattern in the mesh cores is indicative of serpentinization under far from equilibrium conditions (Jamtveit and Hammer, 2012) and also reflect open-system behavior at this stage as indicated by the observed S and Al enrichments.

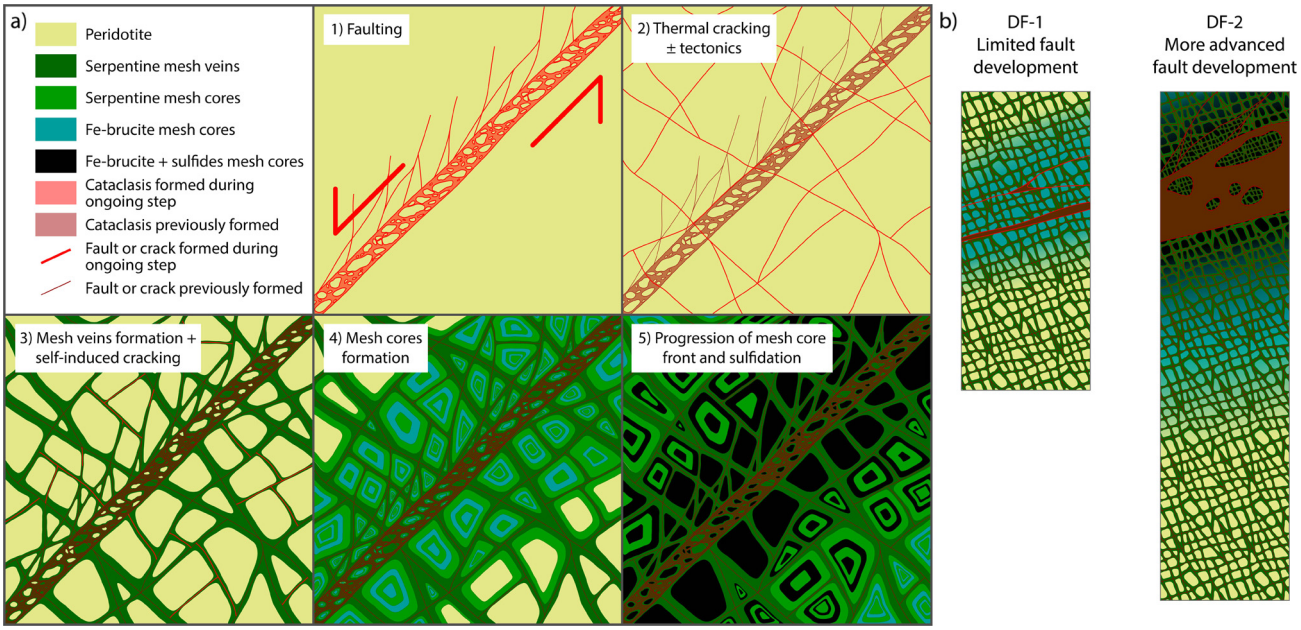

Fig. 9. Conceptual figure for serpentinization from the dark sealed faults. a) Successive steps of fracturing and serpentinization around dark faults. b) Schematic view of the difference in metasomatism associated with difference in fault development as observed in DF-1 and DF-2. Legend is the same as for a). Because of the larger scale than a), oscillatory patterns are not represented.

A model emerges which includes an early stage of serpentinization with associated mesh texture formation. During this stage, the progress of serpentinization leads to clogging of the pore space (Hövelmann et al., 2012) and prevents water supply before the mesh cores are completely hydrated. The result of this stage is observed in sample DF-1 where relict of olivine can still be observed. Following this stage, the porosity is still connected to external fluid sources along the main faults and fractures. Sustained fluid flux then becomes more focused as less favorable pathways are abandoned, leading to metasomatic effects as observed in sample DF-2 where mesh cores in the fault zone are enriched in S and Al and depleted in Si compared to the mesh cores in the wall-rock (step 5 in Fig. 9a and Fig. 9b).

5. Conclusions

Our observations from the Samail ophiolite peridotites emphasize the close link between serpentinization, tectonic stress, and brittle deformation. We describe a family of highly localized and early faults that predates mesh texture formation. Macroscopic and microscopic structures, as well as EBSD observations are consistent with high energy brittle faulting. The faults act as major pathways for water infiltration in the rock even after pervasive fluid infiltration has ceased (i.e., after mesh formation). The formation of oscillatory zoning in replacement for olivine is symptomatic of far from equilibrium reaction conditions, possibly indicative of an irregular fluid supply to the system.

Bulk rock and SIMS analyses show low to moderate enrichment on fluid mobile elements including B, Li, Rb, and U, indicative of fluid-rock interaction in an oceanic environment characterized by relatively low fluid-rock ratios. This is consistent with a model where fluid-rock interactions took place below a thick magmatic crust. The oxygen isotope compositions of mesh serpentine are consistent with medium temperature serpentinization (200-250 °C) at ca. 50 km distance from the active fast spreading ridge.

CRediT authorship contribution statement

Claire Aupart: Investigation, Formal analysis, Data Curation, Writing – original draft.

Luiz Morales: Investigation, Writing – review & editing.

Marguerite Godard: Investigation, Writing – review & editing.

Bjørn Jamtveit: Investigation, Supervision, Funding acquisition, Writing – review & editing.

The Oman DP science team: Resources, Data Curation.

Declaration of competing interest

The authors declare that they have no known competing financial interests or personal relationships that could have appeared to influence the work reported in this paper.

Acknowledgements

This project has been supported by the European Union's Horizon 2020 Research and Innovation Programme [ERC Advanced Grant Agreement n°669972, 'Disequilibrium Metamorphism' ('DIME'), to B. Jamtveit]. The NordSIM facility is jointly funded by the Swedish Museum of Natural History, the Swedish Research Council (infrastructure grant 2017-00671) and the University of Iceland; this is NordSIMS publication #688. This research used samples and/or data provided by the Oman Drilling Project. The Oman Drilling Project (OmanDP) has been possible through comingled funds from the International Continental Scientific Drilling Program (ICDP; Kelemen, Matter, Teagle Lead PIs), the Sloan Foundation – Deep Carbon Observatory (Grant 2014-3-01, Kelemen PI), the National Science Foundation (NSF-EAR-1516300, Kelemen lead PI), NASA – Astrobiology Institute (NNA15BB02A, Templeton PI), the German Research Foundation (DFG: KO 1723/21-1, Koepke PI), the Japanese Society for the Promotion of Science (JSPS no: 16H06347, Michibayashi PI; and KAKENHI 16H02742, Takazawa PI), the European Research Council (Adv: no. 669972; Jamveit PI), the Swiss National Science Foundation (SNF: 20FI21_163073, Früh-Green PI), JAMSTEC, the TAMU-JR Science Operator, and contributions from the Sultanate of Oman Ministry of Regional Municipalities and Water Resources, the Oman Public Authority of Mining, Sultan Qaboos University, CNRS-Univ. Montpellier, Columbia University of New York, and the University of Southampton. We thank Siri Simonsen and Muriel Erambert for their help with

SEM and electronic microprobe data, Thanusha Naidoo, Ibrahim Khaled and Gunborg Bye Fjeld for their help with rock crushing and milling, and Martin Whitehouse and Heejin Jeon for their help and warm welcome into the NordSIM facilities. We thank C. Martin (Géosciences Montpellier) and L. Causse (AETE-ISO facility, OSU-OREME/Université de Montpellier) for their assistance during whole-rock trace element chemical preparation and analysis by quadrupole ICP-MS. We thank three anonymous reviewers for helpful reviews, and A. Webb for editorial handling.

Appendix A. Method for SEM and EBSD analyses

SEM pictures and EDS maps provided in this study have been obtained at the University of Oslo on a dual Bruker Quantax XFlash 30 EDS system with an accelerating voltage of 15 kV. Samples were carbon coated beforehand.

Electron backscatter diffraction (EBSD) orientation maps were acquired in the Scientific Center for Optical and Electron Microscopy (ScopeM), ETH Zürich. The thin section DF-2C was mechanically polished with diamond solutions up to a 0.25 microns grain size and final polishing was performed with an alkaline solution of colloidal silica for 3 minutes on a neoprene substrate. For the EBSD mapping, the sample was coated with 3 nm of C. The maps were acquired in a FEI Quanta 200F with EDAX EBSD/EDS system, using an accelerating voltage of 20 kV, beam current of 8 nA, working distance of 15 mm and step size of 1 micron. After the acquisition, the raw data was cleaned with the software OIM 85, by first performing confidence index (CI) standardization followed by neighbor CI correlation, assuming a minimum CI of 0.1. Afterwards, all the points with CI smaller than 0.1 and detected grain sizes smaller than 10 pixels were removed and not considered in the texture calculations. The crystallographic preferred orientation data was plotted in pole figures using the sample reference frame via the MatLab Toolbox MTEX (version 5.2.8; http://mtex-toolbox.github.io; Bachmann et al., 2010, 2011; Hielscher and Schaeben, 2008).

Appendix B. Methods for whole rock analyses

Samples were crushed and reduced to powders using the facilities of the Geosciences Department of the University of Oslo using an iron plate and a steel mill. Before the crushing, the pyroxene dyke in DF-1 was cut out of the sample.

Trace element concentrations (Li, Sc, Ti, V, Mn, Co, Ni, Cu, Zn, Ga, As, Rb, Sr, Y, Zr, Nb, Cd, Sn, Sb, Cs, Ba, Rare Earth Elements (REE), Hf, Ta, Pb, Th and U) were determined at Géosciences Montpellier (AETE-ISO, OSU OREME, Université de Montpellier, France) using an Agilent 7700X quadrupole ICP-MS. Powdered samples were prepared following the $HF/HClO_4$ procedure described in Ionov et al. (1992) and Godard et al. (2000). The samples were analyzed after a dilution of 1000. Element concentrations were measured by external calibration, except for Nb and Ta that were calibrated by using Zr and Hf, respectively, as internal standards. This technique is an adaptation to ICP-MS analysis of the surrogate calibration method described by Jochum et al. (1990); it aims at avoiding memory effects due to the introduction of concentrated Nb-Ta solutions in the instrument. The Helium cell gas mode of the Agilent 7700X was used to measure Sc, Ti, V, Mn, Co, Ni, Cu, Zn, Ga, As, Sn and Sb while removing polyatomic interferences. Each ICPMS measurement is an average of three runs and its precision is determined by its standard deviation. The uncertainty of analysis was estimated for each sample using the error propagation method described in Godard et al. (2000), which takes into account the precision of the measurements of (i) the instrumental blank, (ii) the procedural blanks and (iii) the sample analysis. Analyses (i) below the instrument detection limit, (ii) for which the contribution of the procedural blank is > 70% or (iii) having uncertainties >50 % were eliminated (noted "not determined"). We also analyzed rock reference materials DTS-2b and UB-N to assess the external precision and accuracy of our analyses. Our results show good agreement between measured values and expected values for the international standards, and reproducibility is generally better than 3% at concentrations > 10 ng/g, and 3-10 % for concentrations less than 10 ng/g. The limits of detection, the procedural blank contributions and the values obtained for rock standards during this study are reported in Supplementary Table S3.

Appendix C. Methods for ion probe analyses

Oxygen isotope composition ($^{18}O/^{16}O$, expressed as $\delta^{18}O_{V\text{-}SMOW}$) and B-concentrations of serpentine minerals were performed *in situ* on gold-coated samples from thin section DF-2C using a large geometry CAMECA IMS 1280 ion microprobe at the NordSIMS ion microprobe laboratory at the Swedish Natural History Museum, Stockholm. The spatial resolution for both measurements was similar at ca. 10-15 µm. For oxygen isotopes, the instrument was operated with a critically focused, 10 µm-rastered, ca. 2nA, Cs+ beam together with low energy electron flooding gun to counteract change build up, and simultaneous detection in two low-noise Faraday detectors, closely following the method reported for analyses of Zircon from the same laboratory (Whitehouse et al., 2017). Polished pieces of lizardite L3431 and antigorite Al06-44A reference materials (kindly provided by D. Rubatto) were co-mounted in the sample holder along with the thin section and used to correct for instrumental mass bias using the $\delta^{18}O$-values of 5.26‰ and 8.22‰, respectively (Scicchitano et al., 2018). Prior to secondary ion mass spectrometry (SIMS) analysis, both materials were imaged unsing high contrast back-scattered electron (BSE) to reveal areas of alteration that were avoided during $\delta^{18}O$ measurements. Matrix bias effects among different serpentine minerals (notably antigorite and lizardite) are relatively small during the same analytical session as the unknown analyses in this study, Al06-44A calibrated against L3441 yielded a 8.38 ± 0.18‰ (1s, n=14), within uncertainty of the expected value. The lizardite reference material was analyzed once every 3 to 5 samples unknowns and yielded a $\delta^{18}O$ reproducibility of ± 0.20‰ (1s, n=32/34).

Boron analyses were performed using a critically focused, 5 µm-rastered, ca. 5nA, O_2^- beam, with $^{11}B^+/^{28}Si^{2+}$ ratios determined by peak jumping $^{11}B^+$ and $^{28}Si^{2+}$ with a mass resolution (M/ΔM) of ca. 2500 into a pulse counting electron multiplier. Two silicate glass reference materials were used for boron analyses. The primary reference, B6 obsidian (203.8 µg/g B, 75.5 wt% SiO_2; Gonfiantini et al., 2003), was analyzed at the beginning and at the end of the measurement session, yielding an uncertainty of ca. 2% (1s) in the $^{11}B/^{28}Si$ ratio. The secondary reference, GOR132-G (17.2 µg/g B, 45.5 wt% SiO_2; Jochum et al., 2006) was analyzed only at the end of the session and yielded a $^{11}B/^{28}Si$ ratio uncertainty of ca. 4% (1s). The estimate of boron concentration uses the equation below assuming ~35.5 wt% SiO_2 in the targeted serpentine minerals based on the electronic microprobe data (Supplementary Table S1-S6):

$$B_{sample}\,(ppm) = \frac{^{11}B}{^{28}Si}_{sample} \cdot [SiO_2]_{sample} \cdot \frac{B_{std}}{[SiO_2]_{std}} \cdot \left(\frac{^{11}B}{^{28}Si}_{std}\right)^{-1}$$

Calculations using the B6 reference material yielded slightly too high values for B concentration in the GOR132-G reference (~20.9 ppm). This is likely an effect of the difference in SiO_2 content between the two glasses as well as a crystallographic difference. Thus, since the GOR132-G glass has silica content closer to the serpentine sample, we renormalized to this material for final B concentration.

Appendix D. Method for the microprobe analyses

Major elements mineral compositions in thin section DF-2C were obtained by wavelength dispersive analysis using a Cameca SX100 electron microprobe at the Department of Geosciences, University of Oslo. Natural minerals and synthetic phases were used as standards. The accelerating voltage was 15 kV, and the beam current varied between 10 and 15 nA. The counting time was 10 s on both peak and background. Data reduction was carried out with the Cameca PAP software package. Analysis of mesh cores and cataclasite matrix were made using a slightly defocused (ca. 5 µm) electron beam to obtain representative average values for these fine-grained heterogeneous materials.

Appendix E. Supplementary material

Supplementary material related to this article can be found online at https://doi.org/10.1016/j.epsl.2021.117137.

References

Agranier, A., Lee, C.-T.A., Li, Z.-X.A., Leeman, W.P., 2007. Fluid-mobile element budgets in serpentinized oceanic lithospheric mantle: insights from B, As, Li, Pb, PGEs and Os isotopes in the Feather River Ophiolite, California. Chem. Geol. 245 (3–4), 230–241. https://doi.org/10.1016/j.chemgeo.2007.08.008.

Aupart, C., Dunkel, K.G., Angheluta, L., Austrheim, H., Ildefonse, B., Malthe-Sørenssen, A., Jamtveit, B., 2018. Olivine grain size distributions in faults and shear zones: evidence for nonsteady state deformation. J. Geophys. Res., Solid Earth 123, 7421–7443. https://doi.org/10.1029/2018JB015836.

Aupart, C., 2020. Mechano-chemical feedbacks during deformation and hydration of peridotites. Doctoral thesis. University of Olso.

Bach, W., Garrido, C.J., Paulick, H., Harvey, J., Rosner, M., 2004. Seawater-peridotite interactions: first insights from ODP Leg 209, MAR 15°N. Geochem. Geophys. Geosyst. 5 (9). https://doi.org/10.1029/2004GC000744.

Bach, W., Paulick, H., Garrido, C.J., Ildefonse, B., Meurer, W.P., Humphris, S.E., 2006. Unraveling the sequence of serpentinization reactions: petrography, mineral chemistry, and petrophysics of serpentinites from MAR 15°N (ODP Leg 209, Site 1274). Geophys. Res. Lett. 33 (13). https://doi.org/10.1029/2006GL025681.

Bachmann, F., Hielscher, R., Schaeben, H., 2010. Texture analysis with MTEX – free and open source software toolbox. Solid State Phenom. 160, 63–68. https://doi.org/10.4028/www.scientific.net/SSP.160.63.

Bachmann, F., Hielscher, R., Schaeben, H., 2011. Grain detection from 2d and 3d EBSD data—specification of the MTEX algorithm. Ultramicroscopy 111 (12), 1720–1733. https://doi.org/10.1016/j.ultramic.2011.08.002.

Boudier, F., Nicolas, A., Ildefonse, B., Jousselin, D., 1997. EPR microplates, a model for the Oman ophiolite. Terra Nova 9 (2), 79–82. https://doi.org/10.1111/j.1365-3121.1997.tb00007.x.

Boudier, F., Nicolas, A., Mainprice, D., 2005. Does anisotropy of thermal contraction control hydrothermal circulation at the moho level below fast spreading oceanic ridges? Int. Geol. Rev. 47 (1), 101–112. https://doi.org/10.2747/0020-6814.47.1.101.

Campbell, A.C., Palmer, M.R., Klinkhammer, G.P., Bowers, T.S., Edmond, J.M., Lawrence, J.R., Casey, J.F., Thompson, G., Humphris, S., Rona, R.A., Karson, J.A., 1988. Chemistry of hot springs on the Mid-Atlantic Ridge. Nature 335, 514–519.

Cannat, M., 1993. Emplacement of mantle rocks in the seafloor at mid-ocean ridges. J. Geophys. Res., Solid Earth 98 (B3), 4163–4172. https://doi.org/10.1029/92JB02221.

Cladouhos, T.T., 1999. Shape preferred orientations of survivor grains in fault gouge. J. Struct. Geol. 21 (4), 419–436. https://doi.org/10.1016/S0191-8141(98)00123-0.

Deschamps, F., Guillot, S., Godard, M., Andreani, M., Hattori, K., 2011. Serpentinites act as sponges for fluid-mobile elements in abyssal and subduction zone environments. Terra Nova 23, 171–178. https://doi.org/10.1111/j.1365-3121.2011.00995.x.

Escartin, J., Hirth, G., Evans, B., 2001. Strength of slightly serpentinized peridotites: implications for the tectonics of oceanic lithosphere. Geology 29 (11), 1023–1026. https://doi.org/10.1130/0091-7613(2001)029<1023:SOSSPI>2.0.CO;2.

Fisher, A.T., 1998. Permeability within basaltic oceanic crust. Rev. Geophys. 36 (2), 143–182. https://doi.org/10.1029/97RG02916.

Godard, M., Jousselin, D., Bodinier, J.-L., 2000. Relationships between geochemistry and structure beneath a palaeo-spreading centre: a study of the mantle section in the Oman Ophiolite. Earth Planet. Sci. Lett. 180, 133–148.

Godard, M., Lagabrielle, Y., Alard, O., Harvey, J., 2008. Geochemistry of the highly depleted peridotites drilled at ODP Sites 1272 and 1274 (Fifteen-Twenty Fracture Zone, Mid-Atlantic Ridge): implications for mantle dynamics beneath a slow spreading ridge. Earth Planet. Sci. Lett. 267 (3–4), 410–425. https://doi.org/10.1016/j.epsl.2007.11.058.

Gonfiantini, R., Tonarini, S., Gröning, M., Adorni-Braccesi, A., Al-Ammar, A.S., Astner, M., Bächler, S., Barnes, R.M., Bassett, R.L., Cocherie, A., Deyhle, A., Dini, A., Ferrara, G., Gaillardet, J., Grimm, J., Guerrot, C., Krähenbühl, U., Layne, G., Lemarchand, D., Meixner, A., Northington, D.J., Pennisi, M., Reitznerová, E., Rodushkin, I., Sugiura, N., Surberg, R., Tonn, S., Wiedenbeck, M., Wunderli, S., Xiao, Y., Zack, T., 2003. Intercomparison of boron isotope and concentration measurements. Part II: evaluation of results. Geostand. Newsl. 27, 41–57. https://doi.org/10.1111/j.1751-908X.2003.tb00711.x.

Hanghøj, K., Kelemen, P.B., Hassler, D., Godard, M., 2010. Composition and genesis of depleted mantle peridotites from the Wadi Tayin Massif, Oman Ophiolite; major and trace element geochemistry, and Os isotope and PGE systematics. J. Petrol. 51 (1–2), 201–227. https://doi.org/10.1093/petrology/egp077.

Hielscher, R., Schaeben, H., 2008. A novel pole figure inversion method: specification of the MTEX algorithm. J. Appl. Crystallogr. 41, 1024–1037. https://doi.org/10.1107/S0021889808030112.

Holm, N.G., Charlou, J.L., 2001. Initial indications of abiotic formation of hydrocarbons in the Rainbow ultramafic hydrothermal system, Mid-Atlantic ridge. Earth Planet. Sci. Lett. 191 (1–2), 1–8. https://doi.org/10.1016/S0012-821X(01)00397-1.

Hövelmann, J., Austrheim, H., Jamtveit, B., 2012. Microstructure and porosity evolution during experimental carbonation of a natural peridotite. Chem. Geol. 334 (December), 254–265. https://doi.org/10.1016/j.chemgeo.2012.10.025.

Ildefonse, B., Nicolas, A., Boudier, F., 1993. Evidence from the Oman ophiolite for sudden stress changes during melt injection at oceanic spreading centres. Nature 366, 673–675. https://doi.org/10.1038/366673a0.

Ionov, D.A., Savoyant, L., Dupuy, C., 1992. Application of the ICP-MS technique to trace element analysis of peridotites and their minerals. Geostand. Newsl. 16 (2), 311–315.

Iyer, K., Rüpke, L.H., Morgan, J.P., 2010. Feedbacks between mantle hydration and hydrothermal convection at ocean spreading centers. Earth Planet. Sci. Lett. 296 (1–2), 34–44. https://doi.org/10.1016/j.epsl.2010.04.037.

Jamtveit, B., Hammer, Ø, 2012. Sculpting rocks by reactive fluids. Geochem. Perspect. 1 (3), 341–481.

Jochum, K.P., Seufert, H.M., Thirwall, M.F., 1990. High-sensitivity Nb analysis by spark-source mass spectrometry (SSMS) and calibration of XRF Nb and Zr. Chem. Geol. 81 (1–2), 1–16.

Jochum, K.P., Stoll, B., Herwig, K., Willbold, M., Hofmann, A.W., Amini, M., Aarburg, S., Abouchami, W., Hellebrand, E., Mocek, B., Raczek, I., Stracke, A., Alard, O., Bouman, C., Becker, S., Dücking, M., Brätz, H., Klemd, R., de Bruin, D., Canil, D., Cornell, D., de Hoog, C.-J., Dalpé, C., Danyushevsky, L., Eisenhauer, A., Gao, Y., Snow, J.E., Groschopf, N., Günther, D., Latkoczy, C., Guillong, M., Hauri, E.H., Höfer, H.E., Lahaye, Y., Horz, K., Jacob, D.E., Kasemann, S.A., Kent, A.J.R., Ludwig, T., Zack, T., Mason, P.R.D., Meixner, A., Rosner, M., Misawa, K., Nash, B.P., Pfänder, J., Premo, W.R., Sun, W.D., Tiepolo, M., Vannucci, R., Vennemann, T., Wayne, D., Woodhead, J.D., 2006. MPI-DING reference glasses for in situ microanalysis: new reference values for element concentrations and isotope ratios. Geochem. Geophys. Geosyst. 7 (2). https://doi.org/10.1029/2005GC001060.

Jousselin, D., Nicolas, A., 2000. Oceanic ridge off-axis deep structure in the Mansah region (Sumail massif, Oman ophiolite). Mar. Geophys. Res. 21, 243–257. https://doi.org/10.1023/A:1026741208295.

Kelemen, P.B., Hirth, G., Shimizu, N., Spiegelman, M., Dick, H.J., 1997. A review of melt migration processes in the adiabatically upwelling mantle beneath oceanic spreading ridges. Philos. Trans. R. Soc. Lond. A, Math. Phys. Eng. Sci. 355 (1723). https://doi.org/10.1098/rsta.1997.0010.

Kelemen, P.B., Matter, J.M., Teagle, D.A.H., Coggon, J.A., 2020, the Oman Drilling Project Science Team. In: Proceedings of the Oman Drilling Project (International Ocean Discovery Program). College Station, TX.

Klein, F., Bach, W., Humphris, S.E., Kahl, W.-A., Jöns, N., Moskowitz, B., Berquó, T.S., 2014. Magnetite in seafloor serpentinite—some like it hot. Geology 42 (2), 135–138. https://doi.org/10.1130/G35068.1.

Malvoisin, B., 2015. Mass transfer in the oceanic lithosphere: serpentinization is not isochemical. Earth Planet. Sci. Lett. 430, 75–85. https://doi.org/10.1016/j.epsl.2015.07.043.

Mariani, E., Crispini, L., Teagle, D.A.H., 2019. Anhydrite deformation and microstructures in the oceanic lower crust: an insight from Samail ophiolite core, Wadi Gideah GT1 Borehole. In: Geophysical Research Abstracts, vol. 21.

McCollom, T.M., Bach, W., 2009. Thermodynamic constraints on hydrogen generation during serpentinization of ultramafic rocks. Geochim. Cosmochim. Acta 73 (3), 856–875. https://doi.org/10.1016/j.gca.2008.10.032.

Mével, C., 2003. Serpentinization of abyssal peridotites at mid-ocean ridges. C. R. Géosci. 335 (10–11), 825–852. https://doi.org/10.1016/j.crte.2003.08.006.

Nicolas, A., Reuber, I., Benn, K., 1988. A new magma chamber model based on structural studies in the Oman ophiolite. Tectonophysics 151 (1–4), 87–105. https://doi.org/10.1016/0040-1951(88)90242-9.

Nicolas, A., Boudier, F., Ildefonse, B., Ball, E., 2000. Accretion of Oman and United Arab Emirates ophiolite – discussion of a new structural map. Mar. Geophys. Res. 21, 147–180. https://doi.org/10.1023/A:1026769727917.

Noël, J., 2018. Etude pétro-structurale et géochimique des processus de serpentinisation et de carbonatation des péridotites de l'ophiolite d'Oman. Doctoral thesis. University of Montpellier.

Paulick, H., Bach, W., Godard, M., De Hoog, J.C.M., Suhr, G., Harvey, J., 2006. Geochemistry of abyssal peridotites (Mid-Atlantic Ridge, 15°20′N, ODP Leg 209): implications for fluid/rock interaction in slow spreading environments. Chem. Geol. 234 (3–4), 179–210. https://doi.org/10.1016/j.chemgeo.2006.04.011.

Peters, D., Bretscher, A., John, T., Scambelluri, M., Pettke, T., 2017. Fluid-mobile elements in serpentinites: constraints on serpentinisation environments and element cycling in subduction zones. Chem. Geol. 466, 654–666. https://doi.org/10.1016/j.chemgeo.2017.07.017.

Plümper, O., Røyne, A., Magraso, A., Jamtveit, B., 2012. The interface-scale mechanism of reaction-induced fracturing during serpentinization. Geology 40 (12), 1103–1106. https://doi.org/10.1130/G33390.1.

Rioux, M., Garber, J., Bauer, Ann, Bowring, S., Searle, M., Kelemen, P., Hacker, B., 2016. Synchronous formation of the metamorphic sole and igneous crust of the Semail ophiolite: new constraints on the tectonic evolution during ophiolite formation from high-precision U–Pb zircon geochronology. Earth Planet. Sci. Lett. 451, 185–195. https://doi.org/10.1016/j.epsl.2016.06.051.

Rospabé, M., Benoit, M., Ceuleneer, G., Kaczmarek, M.-A., Hodel, F., 2019. Melt hybridization and metasomatism triggered by syn-magmatic faults within the Oman ophiolite: a clue to understand the genesis of the dunitic mantle-crust transition zone. Earth Planet. Sci. Lett. 516, 108–121. https://doi.org/10.1016/j.epsl.2019.04.004.

Saccocia, P.J., Seewald, J.S., Shanks, W.C., 2009. Oxygen and hydrogen isotope fractionation in serpentine–water and talc–water systems from 250 to 450 °C, 50 MPa. Geochim. Cosmochim. Acta 73 (22), 6789–6804. https://doi.org/10.1016/j.gca.2009.07.036.

Sammis, C., King, G., Biegel, R., 1987. The kinematics of gouge deformation. Pure Appl. Geophys. 125, 777–812. https://doi.org/10.1007/BF00878033.

Schuiling, R.D., 1964. Serpentinization as a possible cause of high heat-flow values in and near the oceanic ridges. Nature 201, 807–808. https://doi.org/10.1038/201807b0.

Scicchitano, M.R., Rubatto, D., Hermann, J., Shen, T., Padrón-Navarta, J.A., Williams, I.S., Zheng, Y.-F., 2018. In situ oxygen isotope determination in serpentine minerals by ion microprobe: reference materials and applications to ultrahigh-pressure serpentinites. Geostand. Geoanal. Res. 42 (4), 459–479. https://doi.org/10.1111/ggr.12232.

Steacy, S.J., Sammis, C.G., 1991. An automaton for fractal patterns of fragmentation. Nature 353, 250–252. https://doi.org/10.1038/353250a0.

Stein, C.A., Stein, S., 1994. Constraints on hydrothermal heat flux through the oceanic lithosphere from global heat flow. J. Geophys. Res., Solid Earth 99 (B2), 3081–3095. https://doi.org/10.1029/93JB02222.

Sun, S.S., McDonough, W.F., 1989. Chemical and isotopic systematics of oceanic basalts: implications for mantle composition and processes. In: Saunders, A.D., Norry, M.J. (Eds.), Magmatism in the Ocean Basins. London: Geological Society of London, pp. 313–345.

Tolstoy, M., Waldhauser, F., Bohnenstiehl, D.R., Weekly, R.T., Kim, W.-Y., 2008. Seismic identification of along-axis hydrothermal flow on the East Pacific Rise. Nature 451, 181–184. https://doi.org/10.1038/nature06424.

Toomey, D.R., Jousselin, D., Dunn, R.A., Wilcock, S.D., Detrick, R.S., 2007. Skew of mantle upwelling beneath the East Pacific Rise governs segmentation. Nature 446, 409–414. https://doi.org/10.1038/nature05679.

Viti, C., Mellini, M., 1998. Mesh textures and bastites in the Elba retrograde serpentinites. Eur. J. Mineral. 10 (6), 1341–1360. https://doi.org/10.1127/ejm/10/6/1341.

Whitehouse, M.J., Nemchin, A.A., Pidgeon, R.T., 2017. What can Hadean detrital zircon really tell us? A critical evaluation of their geochronology with implications for the interpretation of oxygen and hafnium isotopes. Gondwana Res. 51, 78–91. https://doi.org/10.1016/j.gr.2017.07.007.

Zihlmann, B., Müller, S., Coggon, R.M., Koepke, J., Garbe-Schönberg, D., Teagle, D.A.H., 2018. Hydrothermal fault zones in the lower oceanic crust: an example from Wadi Gideah, Samail ophiolite, Oman. Lithos 323, 103–124. https://doi.org/10.1016/j.lithos.2018.09.008.